

Template-Free Preparation of Mesoporous Fe₂O₃ and Its Application as Absorbents

Chichao Yu, Xiaoping Dong, Limin Guo, Jiangtian Li, Fei Qin, Lingxia Zhang, Jianlin Shi,* and Dongsheng Yan

State Key Laboratory of High Performance and Superfine Microstructure, Shanghai Institute of Ceramics, Chinese Academy of Sciences, 1295 Ding-xi Road, Shanghai, 200050 (China).

Received: May 15, 2008; Revised Manuscript Received: July 2, 2008

In this paper, we present an easy template-free route to synthesize mesoporous Fe₂O₃ with a high surface area of 111 m²/g and narrow pore distribution at 4.4 nm. This strategy has significant advantages comparing to the traditional templating routes in performance/price ratio and flexibility of procedures, and the mesoporous materials can be manufactured in quantity scale. The prepared mesoporous materials were used as an adsorbent to dispose of the Congo red containing wastewater, and they exhibited more favorable adsorptive properties than the commercial metal oxide powders with low surface area.

Introduction

Due to their unique catalytic, electrochemical, magnetic and adsorptive properties, mesoporous transition metal oxides have been extensively studied in the past decade.^{1–4} However, the synthesis of mesoporous transition metal oxides is much more difficult than mesoporous silica. In general, the typical synthetic strategy of mesoporous materials involves the use of soft templates^{5–7} (usually surfactants, e.g., an alkyl amine, for mesoporous silica, zirconia, etc.) or hard templates^{8–10} (usually mesoporous silica or carbon, as the template for other mesoporous materials). The sparsity of appropriate metallic precursors limits the development of soft templating methods to prepare most kinds of mesoporous transition metal oxides, while the hard templating methods usually involve multistep processes and sometimes will lead to the loss of pore structure during the removal of hard templates.¹¹ Recently, we proposed a novel strategy to synthesize mesoporous nonsiliceous materials without the help of template by a controlled thermal decomposition of low-cost metal salts which can be extended to synthesize a number of mesoporous metal oxides. In such an approach, mesopores are generated via the thermal decomposition of the salt precursors from micrometer sized polyhedron particles, which is totally different from the mechanisms of cooperative assembly from the starting molecular species commonly under the presence of structure directing templates. We used basic sulfate precursors to prepare mesoporous Al₂O₃, TiO₂ and ZrO₂, and oxalate precursors to prepare mesoporous Mn₂O₃,^{12,13} NiO.¹² All as-synthesized metal oxides with well-defined pore structures have larger surface area than their counterparts prepared by templating methods. Therefore, it is apparent that such a strategy of synthesizing mesoporous metal oxides is superior to traditional templating methods in industrial manufacturing when taking the performance/price ratio and flexibility of procedures into consideration.

Iron oxides are particularly important because of their applications in magnetic storage, catalysis, absorption and rechargeable lithium batteries, which have been reported to be enhanced significantly if the materials are in nanoscale.^{14–18} Hematite (α -Fe₂O₃) is the most stable iron oxide under ambient conditions with virtues of low cost and high resistance to

corrosion. There are a lot of literature reporting on the preparation of porous α -Fe₂O₃ with mesoporous structures using soft^{19–21} and hard^{22,23} template methods. However, soft template methods inevitably resulted in amorphous frameworks, and hard templating methods are usually complicated and time-consuming. Herein, the template-free strategy is employed to synthesize mesoporous α -Fe₂O₃ with high surface area and well-controlled pore structure, and the adsorption property toward Congo red is discussed while comparing with other metal oxides of different surface areas.

Experimental Details

Materials Preparation. A typical preparation procedure for metal oxalate precursor is described as follows: FeSO₄·7H₂O and dioctylsulfosuccinate (AOT) were dissolved in water at 80 °C in oil bath with stirring for at least 2 h; then oxalic acid solution (with a little phosphoric acid in it) was slowly dropped into the former solution. The molar ratio of FeSO₄·7H₂O: oxalic acid: AOT was fixed at 1:0.6:0.2 in the experiments. Yellow precipitates yielded during the process, and then the precipitated products were quickly cooled down by ice water, then separated by centrifugation, subsequently washed by deionized water and ethanol several times, and dried in air overnight. The as-prepared precipitate was calcined at 250, 270 and 300 °C, respectively, and the corresponding decomposed samples were labeled as F1, F2, and F3.

Congo Red Treatment. A 60 mg amount of sample F2 (calcined at 270 °C) was added into 40 mL of a Congo red solution with a concentration of 100 mg/L under stirring at a rate of 150 rpm. At several time intervals, small amounts of the liquid were taken to be analyzed by UV–vis absorption spectroscopy after being diluted by 5 times. The same experiments are performed on microporous manganese oxide¹² and commercial low surface area α -Fe₂O₃ and MnO₂ materials.

Characterization. XRD patterns were recorded on a Rigaku D/Max 2200PC diffractometer using Cu K α radiation at 40 kV and 40 mA. Nitrogen adsorption/desorption isotherms at 77 K were measured on a Micromeritics TriStar 3000 porosimeter. All samples were outgassed at 100 °C for 6 h under flowing nitrogen before measurements. The specific surface areas were calculated with the BET (Brunauer–Emmet–Teller) methods. Pore size and pore size distribution (PSD) plots were obtained

* Corresponding author. E-mail: jlshi@sunm.shenc.ac.cn.

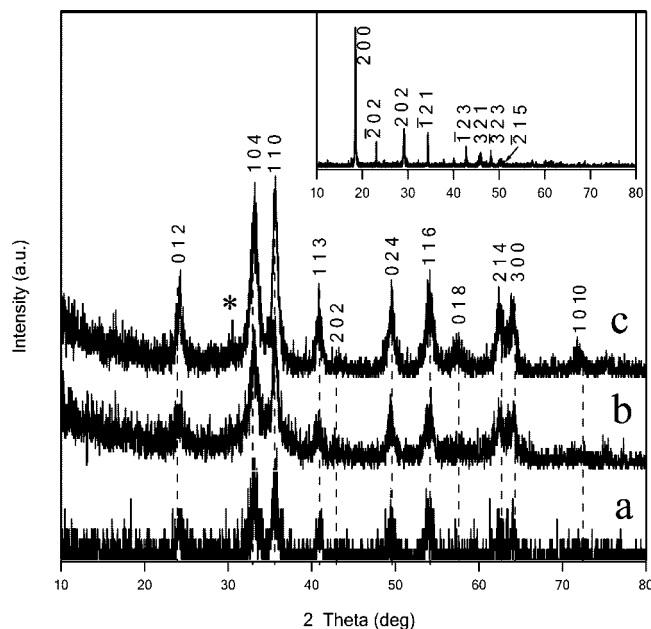


Figure 1. XRD patterns of iron oxalate dihydrate (inset) and iron oxides calcined at different temperatures of 250 °C (a), 270 °C (b), and 300 °C (c) (*: γ -Fe₂O₃).

by BJH method using the cylindrical pore model. FETEM (field emission transmission electron microscopy) analysis was conducted on a JEOL 200CX electron microscope operated at 200 KV. FE-SEM (field emission scanning electron microscopy) analysis was performed on a JEOL JSM6700F electron microscope. TG-DSC measurements were conducted using a NETZSCH STA 449C apparatus with an air flow of 20 mL/min and a heating rate of 10 K/min. UV-vis absorption spectra were conducted using a UV-3101PC instrument manufactured by Shimadzu Corporation.

Results and Discussion

Characterization of Mesoporous Fe₂O₃. From the results of XRD analysis (Figure 1, inset), the as-synthesized precursor is well crystallized with the peak positions and relative intensities coinciding well with the standard XRD pattern of iron oxalate dihydrate. XRD patterns in Figure 1a to Figure 1c are for the calcined samples, and the pronounced peaks at (012), (104) and (110) illustrate that the main phase in the calcined samples at different temperatures from 250 to 300 °C is well crystallized Fe₂O₃ in the form of rhombohedral hematite ($a = 5.038$ Å, $c = 13.772$ Å) similar to the record in JCPDS No.24-0072. However, contrary to the standard card, the (104) peak intensity is lower than that of (110) peak. The (110) peak position is at 35.6 ° while the strongest peak (206) of maghemite is at 35.3 °. The (206) peak of maghemite superposing on the (110) peak of hematite makes the intensity around 35° stronger than that of (104) peak. In the sample calcined at relatively high temperature of 300 °C, the peak at 30.2 ° attributed to γ -Fe₂O₃ can be clearly observed which is not distinct in samples of F1 and F2. The products can be mainly identified as α -Fe₂O₃, with a trace amount of maghemite. Calculated by Scherer's equation, the crystallite sizes of F1, F2 and F3 are 8.9 nm, 9.8 and 12.5 nm, respectively. The roughness of the diffraction peaks caused difficulties in determining the accurate values of full width at half-maxima (fwhm), so the data deduced from Scherer's equation may not represent the accurate crystallite sizes. However, a trend of the size increase of Fe₂O₃ crystallites at

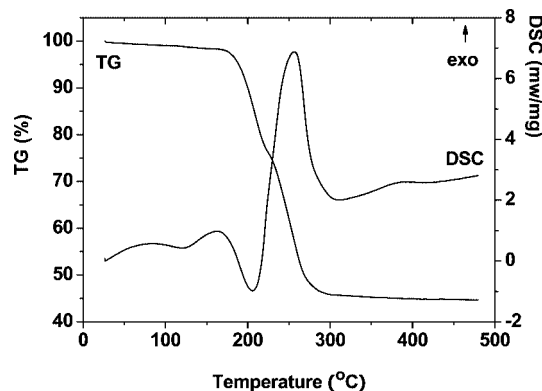


Figure 2. TG and DSC curves of prepared iron oxalate dihydrate.

the elevated heating temperatures can be clearly seen from the data. All calcined Fe₂O₃ samples share the same peak positions, though the peak intensities are different from each other demonstrating the crystallite growth of Fe₂O₃ at elevated calcination temperatures.

TG-DSC analysis of the iron oxalate dihydrate demonstrates the decomposition of the precursor during the heating process (Figure 2). The main endothermal and exothermal peaks are at 200 and 255 °C, respectively, corresponding to the loss of structural water and the decomposition of the oxalate group. The dehydration process of structural water cannot be distinguished clearly from the decomposition of the oxalate group as the two processes took place immediately one after the other. However from the DSC curve, approximately one can infer that the dehydration process took place below 210 °C, where there is an endothermal peak in DSC curves, and the oxalate group decomposes at about 255 °C, where a strong exothermal peak is apparent.

Figure 3 shows SEM and TEM figures of calcined iron oxide at 270 °C. SEM picture (Figure 3A) shows that the crystallized Fe₂O₃ particles are mostly in cubic-shaped polyhedron form of several micrometers in size with few cracks on the surface. Those cracks on the surface of the calcined particle were mainly formed by the release of a mass of gases from the interior which is about 55 wt % of the as-prepared precursor particles, as can be estimated from the DSC curve in Figure 2. The particles experienced limited shrinkage during calcination and kept the regular morphology from its precursor. Considering a large volume of gases released out from the precursor particles with limited dimension shrinkage during calcination, there must be a significant porosity left inside the particles. TEM image demonstrates that the calcined samples are porous materials. Figure 3B shows homogeneous worm-like pores sized of 4–5 nm distributed within the whole particle. Those mesopores are generated via a large quantity of gases (55 wt %) released from the precursor particles, which leaves corresponding voids within the micrometer sized polyhedron oxalate particles during the thermal decomposition. The pores are formed by adjacent crystallized primary particles of several nanometers in the interior of the micrometer sized particles. Samples F1, F2, and F3 are in the same morphology inherited from the precursor with similar porosity but slightly different pore sizes. The crystallized primary particles within the micrometer sized particles are in nanometer scale as can be estimated from the TEM image, the average crystallite size is around 10 nm as roughly calculated with Scherer's equation.

Nitrogen adsorption-desorption isotherm (at 77 K) is employed to determine the pore size distribution of porous α -Fe₂O₃, the results of the measurements are showed in Figure 4 and

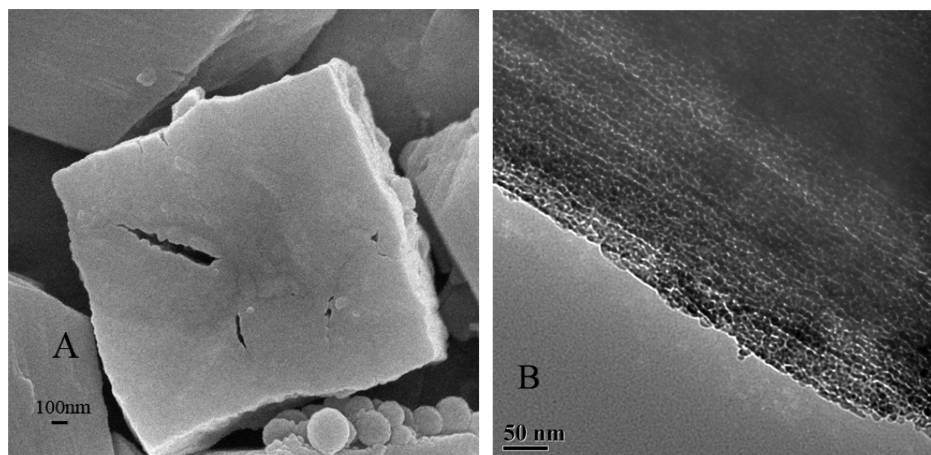


Figure 3. (A) SEM image and (B) TEM image of calcined Fe_2O_3 (270 °C).

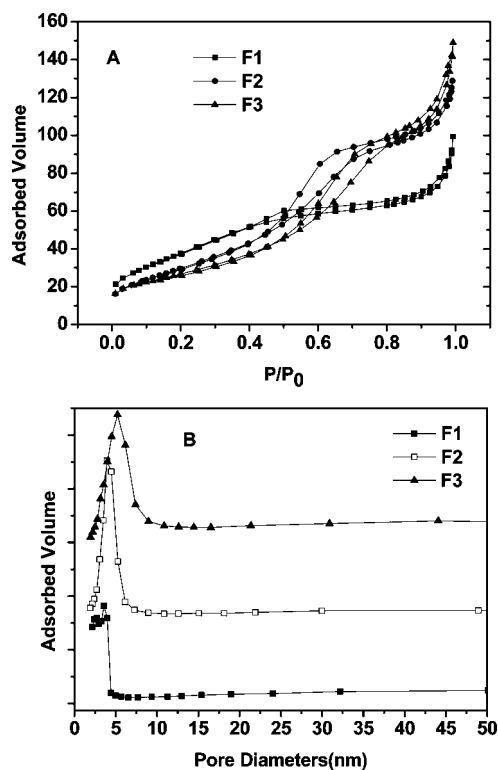


Figure 4. (A) Nitrogen adsorption–desorption isotherms of calcined mesoporous $\alpha\text{-Fe}_2\text{O}_3$ at different temperatures. (B) Corresponding PSD plots calculated from the desorption branches.

TABLE 1: Pore Structural Parameters of Samples F1, F2, and F3

sample	BET surface area ($\text{m}^2 \text{g}^{-1}$)	d_{BJH} (nm)	pore volume ($\text{cm}^3 \text{g}^{-1}$)
F1	131	4.4	0.122
F2	111	4.4	0.179
F3	96	5.2	0.196

summarized in Table 1. In Figure 4A, all samples calcined at different temperatures have typical Langmuir IV type curves with a hysteresis loop, which suggests that the obtained Fe_2O_3 samples are mesoporous materials. The hysteresis loop of F1 begins from $P/P_0 = 0.4$ while those of F2 and F3 from $P/P_0 = 0.5$, illustrating that F2 and F3 have slightly larger pores than F1. Due to Oswald ripening,²⁴ Fe_2O_3 particles grow larger at elevated calcination temperatures which leads to simultaneously increased pore size and broadened pore size distributions.

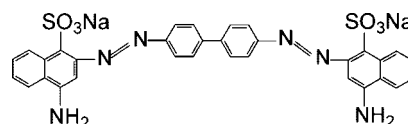


Figure 5. Molecular structure of Congo red.

Meanwhile, the pore volume increases from $0.122 \text{ cm}^3/\text{g}$ to $0.179 \text{ cm}^3/\text{g}$ to $0.196 \text{ cm}^3/\text{g}$ for F1, F2, and F3, respectively. The pore size distribution (PSD) plots calculated from the desorption branches of the nitrogen sorption isotherms are shown in Figure 4B. The PSD curve of F1 demonstrates two differently sized pores in the sample: 2.7 and 4.4 nm. With the increase of calcination temperature, smaller pores would be eliminated by Oswald ripening, while bigger pores grew even bigger. The PSD curves of F2 and F3 show that the pore sizes at the maximum probabilities are around 4.4 and 5.3 nm, respectively. This situation is very similar to our previous work on mesoporous nickel oxides,¹² which also had a bimodal pore size distribution at relatively low calcining temperatures and the pores of smaller size disappeared at elevated temperatures. Due to the smaller pore size, F1 reaches the highest surface area of $131 \text{ m}^2/\text{g}$, while F2 and F3 are 111 and $96 \text{ m}^2/\text{g}$, respectively, which are lower than the mesoporous Fe_2O_3 prepared by hard templating method ($210 \text{ m}^2/\text{g}$),²⁵ but much higher than most of Fe_2O_3 prepared by other approaches. The optimal calcination temperature should be $270 \text{ }^\circ\text{C}$ where the mesoporous Fe_2O_3 sample shows relatively high surface area and well defined pore size distribution. In addition, the other key fact to obtain well-defined pore structure is moderately slow heating rate which was set at $1 \text{ }^\circ\text{C}/\text{min}$.

Application in Waste Water Treatment. Transition metal oxides are commonly used as adsorbents and/or catalysts to remove organic pollutants from wastewater by adsorption and subsequently catalytic combustion at relatively low temperatures.^{26–28} In this paper, we give an example of the potential application of the as-prepared mesoporous Fe_2O_3 to be used as an adsorbent in the wastewater treatment. Congo red (its structure as shown in Figure 5), which is a common dye in textile industry, was selected as the organic contaminant in the wastewater. In the solution, Congo red is adsorbed onto the metal oxide surface by coordination effect between metal ions and amine groups at the ends of Congo red molecules. So it is apparent that metal oxides with the higher surface area can adsorb more Congo red molecules.

UV–vis absorption spectroscopy was used to record the adsorption behavior of the solution after treatment (Figure 6A). The characteristic light absorption of Congo red at 500 nm was

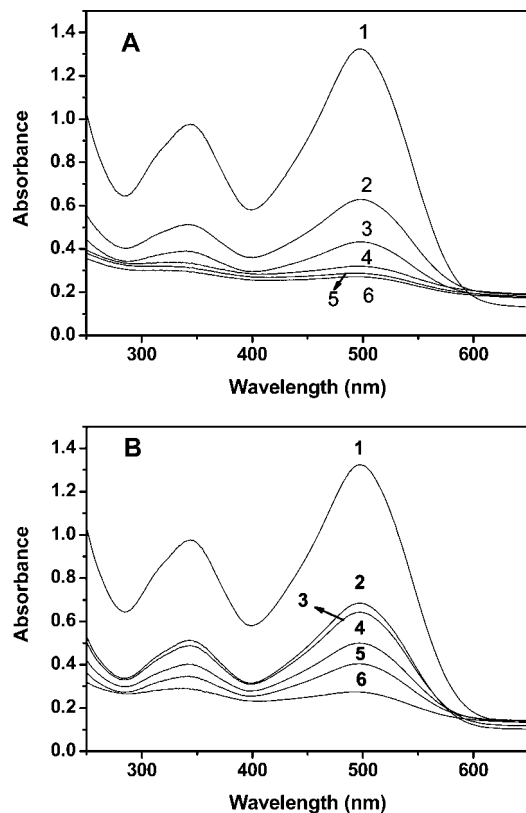


Figure 6. UV-vis absorption spectra of Congo red solutions diluted by 5 times after treated with mesoporous Fe₂O₃ (A) and microporous manganese oxides (B) at different time intervals of (1) 0, (2) 5, (3) 10, (4) 30, (5) 60, and (6) 120 min.

chosen to monitor the process of adsorption, and C_t was used to characterize the relative adsorptive capacity ($C_t = C/C_0$, t is time intervals, C_0 is the initial concentration of Congo red, and C is the current concentration after treatment). When treated with the mesoporous α -Fe₂O₃ for 1 h, the C_{60} value was 21%, and the value decreased slightly to 20% with the disposal time extended to 120 min. The whole adsorption process can be divided into two stages, in the first stage, Congo red was immediately adsorbed within 5 min ($C_5 = 47.5\%$), and in the following second stage beginning from 5 to 60 min, Congo red molecules were adsorbed steadily ($C_{60} = 21\%$). This means that the first stage is a quick adsorption within about 5 min, and the subsequent second stage has a steady absorption in between 5 to 60 min. After 60 min the adsorption becomes saturated and a saturation adsorption capacity is calculated to be 53 mg/g. When a double dose of mesoporous Fe₂O₃ was used to treat the Congo red contained wastewater, the organic contaminant after the treatment could no longer be detected by the UV-vis absorption spectroscopy, which implies that mesoporous Fe₂O₃ could adsorb almost all the organic contamination in the wastewater when excess amount of the adsorbents were used.

For a comparison, microporous manganese oxide (Mn₂O₃) prepared in our previous work,¹² and commercial α -Fe₂O₃ and MnO₂, were used to remove Congo red in wastewater. The UV-vis results for the Congo red solution treated with microporous manganese oxides are shown in Figure 6B. Compared with mesoporous α -Fe₂O₃, the absorption rate for Congo red is much slower at the beginning (0–10 min), probably due to the much smaller micropores of manganese oxides (around 1 nm) than the mesopores of present mesoporous Fe₂O₃ (around 4.4 nm). On the basis of Knudsen's diffusivity model,^{29,30} smaller pores cause more collisions between fluid

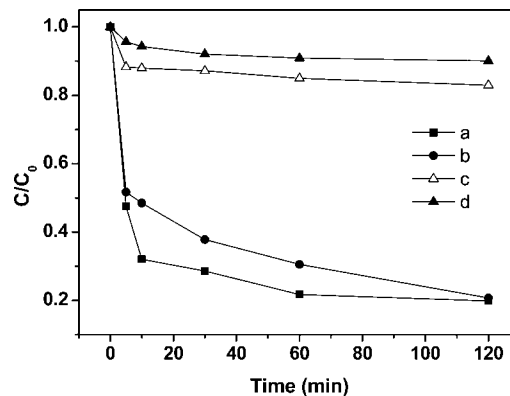


Figure 7. Adsorption capacities for Congo red with as-prepared Fe₂O₃ (a), previously prepared manganese oxides¹² (b), and commercial α -Fe₂O₃ (c) and MnO₂ (d).

TABLE 2: Diffusion Coefficients of Different Adsorbents

	mesoporous Fe ₂ O ₃	microporous manganese oxide	commercial α -Fe ₂ O ₃	commercial MnO ₂
$K_d \times 10^{-2}$ (mg/L)	6.08	5.75	0.30	0.17

and pore-walls leading to the reduced mean free paths, which is supported by the fact in the present study that Congo red solution has faster diffusion rate in mesoporous Fe₂O₃ than in microporous manganese oxide. However, given long enough time for the adsorption, a final equivalent saturation adsorption capacity can be reached in 120 min. The lower adsorption rate of microporous manganese oxide is due to the retarded diffusion kinetics of Congo red molecules in the micropores, while the high surface area (283 m²/g) and the pore volume of the materials ensure its high adsorption capacity similar to that of mesoporous Fe₂O₃. The commercial transition metal oxides (Figure 7, parts c and d) show much lower efficiency in removing Congo red from wastewater, and the saturation adsorption capacities are 11 and 7 mg/g for commercial Fe₂O₃ and MnO₂, respectively, mainly due to their low surface areas (1.04 and 0.58 m²/g for commercial Fe₂O₃ and MnO₂, respectively). The Congo red diffusion coefficient (K_d) was employed to evaluate the effectiveness of the adsorbents,³¹ which was calculated based on the equation of $K_d = ((C_e - C_0)/C_0) \times (V/M)$, where V is the volume of the solution (mL), M is the mass of the adsorbents (g), and C_e is the equilibrium (final) concentration of the Congo red in solution (mg/L). Table 2 summarized K_d values for different adsorbents. The K_d values of mesoporous Fe₂O₃ (608 mg/L) and microporous manganese (575 mg/L) are greatly larger than 100 mg/L, which is the minimal K_d value requested for a successful separation process. Comparatively, the K_d values of the commercial α -Fe₂O₃ and MnO₂ powders are 30 and 17 mg/L, respectively, much smaller than 100 mg/L. From the above discussion, the prepared mesoporous Fe₂O₃ and microporous Mn₂O₃ with their K_d values around 600 mg/L, and together with their advantages of easy preparation and high performance/price ratio, would be highly promising candidate to be applied in the water treatment for the environmental protection.

Conclusion

In summary, an easy oxalate decomposition strategy with controlled morphology and heating rate without using template has been developed to prepare mesoporous Fe₂O₃ materials with high surface area (111 m²/g) and well defined pore size

distribution maximized at 4–5 nm. Mesoporous Fe₂O₃ prepared by such a simple, time-saving and low cost route has relatively high surface area and narrow pore distribution as compared to the similar nanomaterials by other chemical routes, which means that it is more suitable for large-scale manufacture in industrial applications. The performance for the Congo red removal of the prepared mesoporous Fe₂O₃ demonstrates that this material is a very promising candidate as absorbents for wastewater treatment. The other application studies of the mesoporous materials prepared by this facile salt decomposition strategy are under progress.

Acknowledgment. This work was supported by the Natural Foundation of China (Grants 20633090, 50702072, and 20571081).

References and Notes

- (1) Srivastava, D. N.; Perkash, N.; Gedanken, A.; Felner, I. *J. Phys. Chem. B* **2002**, *106*, 1878.
- (2) Chen, H. R.; Dong, X. P.; Shi, J. L.; Zhao, J. J.; Hua, Z. L.; Gao, J. H.; Ruan, M. L.; Yan, D. S. *J. Mater. Chem.* **2007**, *17*, 855.
- (3) He, X.; Trudeau, M.; Antonelli, D. *J. Mater. Chem.* **2003**, *13*, 75.
- (4) Izumi, Y.; Masih, D.; Aika, K.; Seida, Y. *Microporous Mesoporous Mater.* **2007**, *99*, 355.
- (5) Yang, P. D.; Zhao, D. Y.; Margolese, D. I.; Chmelka, B. F.; Stucky, G. D. *Nature* **1998**, *396*, 152.
- (6) MacLachlan, M. J.; Coombs, N.; Ozin, G. A. *Nature* **1999**, *397*, 681.
- (7) Tian, B.; Liu, X.; Yu, C.; Fan, J.; Wang, L.; Xie, S.; Stucky, G. D.; Zhao, D. *Nat. Mater.* **2003**, *2*, 159.
- (8) Jiao, F.; Harrison, A.; Hill, A. H.; Bruce, P. G. *Adv. Mater.* **2007**, *19*, 4063.
- (9) Jiao, F.; Hill, A. H.; Harrison, A.; Berko, A.; Chadwick, A. V.; Bruce, P. G. *J. Am. Chem. Soc.* **2008**, *130*, 5262.
- (10) Jiao, F.; Jumas, J. C.; Womes, J.; Chadwick, A. V.; Harrison, A.; Bruce, P. G. *J. Am. Chem. Soc.* **2006**, *128*, 12905.
- (11) Tiemann, M. *Chem. Mater.* **2008**, *20*, 961.
- (12) Yu, C. C.; Zhang, L. X.; Shi, J. L.; Zhao, J. J.; Gao, J. H.; Yan, D. S. *Adv. Funct. Mater.* **2008**, *18*, 1544.
- (13) Yu, C. C.; Shi, J. L.; Yan, D. S. *Chem. Lett.* **2007**, *36*, 1502.
- (14) Bruce, P. G. *Solid. State. Sci.* **2005**, *7*, 1456.
- (15) Ziolo, R. F.; Giannelis, E. P.; Weinstein, B. A.; Ohoro, M. P.; Ganguly, B. N.; Mehrotra, V.; Russell, M. W.; Huffman, D. R. *Science* **1992**, *257*, 219.
- (16) Fei, J. B.; Cui, Y.; Yan, X. H.; Qi, W.; Yang, Y.; Wang, K. W.; He, Q.; Li, J. B. *Adv. Mater.* **2008**, *20*, 452.
- (17) Chen, J.; Xu, L.; Li, W. Y.; Gou, X. L. *Adv. Mater.* **2005**, *17*, 582.
- (18) Larcher, D.; Masquelier, C.; Bonnin, D.; Chabre, Y.; Masson, V.; Leriche, J. B.; Tarascon, J. M. *J. Electrochem. Soc.* **2003**, *150*, A133.
- (19) Malik, A. S.; Duncan, M. J.; Bruce, P. G. *J. Mater. Chem.* **2003**, *13*, 2123.
- (20) Long, J. W.; Logan, M. S.; Rhodes, C. P.; Carpenter, E. E.; Stroud, R. M.; Rolison, D. R. *Am. Chem. Soc.* **2004**, *126*, 16879.
- (21) Jiao, F.; Bruce, P. G. *Angew. Chem., Int. Ed.* **2004**, *43*, 5958.
- (22) Tian, B.; Liu, X.; Solovyov, L. A.; Liu, Z.; Yang, H.; Zhang, Z.; Xie, S.; Zhang, F.; Tu, B.; Yu, C.; Terasaki, O.; Zhao, D. *Am. Chem. Soc.* **2004**, *126*, 865.
- (23) Kong, A. G.; Wang, H. W.; Li, J.; Shan, Y. K. *Mater. Lett.* **2008**, *62*, 943.
- (24) Zeng, H. C. *J. Mater. Chem.* **2006**, *16*, 649.
- (25) Jiao, F.; Harrison, A.; Jumas, J.; Chadwick, A. V.; Kockelmann, W.; Bruce, P. G. *J. Am. Chem. Soc.* **2006**, *128*, 5468.
- (26) Klihanov, A. M. *Science* **1983**, *221*, 259.
- (27) Zhong, L. S.; Hu, J. S.; Liang, H. P.; Cao, A. M.; Song, W. G.; Wan, L. J. *Adv. Mater.* **2006**, *18*, 2426.
- (28) Fryxell, G. E.; Cao, G. Z. *Environmental Applications of Nanomaterials ICP* **2007**.
- (29) Arya, G.; Chang, H. C.; Maginn, E. J. *Phys. Rev. Lett.* **2003**, *19*, 026102.
- (30) Malek, K.; Coppens, M. O. *J. Chem. Phys.* **2003**, *119*, 2801.
- (31) Wu, P.; Xu, Z. *Ind. Eng. Chem. Res.* **2005**, *44*, 816.

JP8044466